Fusion Engineering and Design 84 (2009) 2158–2166

Contents lists available at ScienceDirect

Fusion Engineering and Design

journal homepage: www.elsevier.com/locate/fusengdes

Transient thermal hydraulic modeling and analysis of ITER divertor plate system

Salah El-Din El-Morshedy[a,b,*], Ahmed Hassanein[c]

[a] Argonne National Laboratory, Argonne, IL, USA
[b] Atomic Energy Authority, Cairo, Egypt
[c] Purdue University, West Lafayette, IN, USA

ARTICLE INFO

Article history:
Received 14 September 2008
Received in revised form 26 February 2009
Accepted 26 February 2009
Available online 26 April 2009

Keywords:
Thermal hydraulics
Safety
Fusion
ITER divertor

ABSTRACT

A mathematical model has been developed/updated to simulate the steady state and transient thermal-hydraulics of the International Thermonuclear Experimental Reactor (ITER) divertor module. The model predicts the thermal response of the armour coating, divertor plate structural materials and coolant channels. The selected heat transfer correlations cover all operating conditions of ITER under both normal and off-normal situations. The model also accounts for the melting, vaporization, and solidification of the armour material. The developed model is to provide a quick benchmark of the HEIGHTS multidimensional comprehensive simulation package. The present model divides the coolant channels into a specified axial regions and the divertor plate into a specified radial zones, then a two-dimensional heat conduction calculation is created to predict the temperature distribution for both steady and transient states. The model is benchmarked against experimental data performed at Sandia National Laboratory for both bare and swirl tape coolant channel mockups. The results show very good agreements with the data for steady and transient states. The model is then used to predict the thermal behavior of the ITER plasma facing and structural materials due to plasma instability event where 60 MJ/m^2 plasma energy is deposited over 500 ms. The results for ITER divertor response is analyzed and compared with HEIGHTS results.

1. Introduction

The worldwide research and development effort in fusion energy is motivated by the aspiration that a properly designed and constructed fusion reactor would allow harnessing the source of the sun's energy in a way that will either eliminate or greatly improve upon the disadvantages associated with other current energy sources. The International Thermonuclear Experimental Reactor (ITER) is a collaborative international project to design, build and operate a 500 MW fusion machine. The project involving the world's leading fusion energy programs: the European Union, China, India, Japan, S. Korea, Russia and United States. The primary objective of ITER is demonstrating the scientific and technological feasibility of fusion energy for peaceful purposes [1]. In fusion tokamak reactors, such as ITER, the plasma facing components (PFCs) are exposed to one sided heat fluxes that are created by energetically charged particles and photons striking the PFC surfaces. The divertor modules in a tokamak are used to remove exhaust from the burning plasma and so receive the highest heat loads of the PFCs. In order to increase the heat removal capability of the divertor, the device may have several individual coolant channels defined as divertor plates that run parallel to each other and are assembled as a unit. The divertor plates always have a protective armour such as beryllium or tungsten tiles to limit plasma damage to the copper heat sink. During normal operations, ITER PFCs are expected to absorb an average heat load of 2 MW/m^2 while the divertor plates will be designed to absorb average heat flux of 5 MW/m^2 [2]. In order to insure reactor reliability, the reactor cooling system needs to be designed to withstand the most probable and highest heat loads from the plasma, with a substantial margin of safety against heat sink burnout.

Light water is a solution for ITER coolant. Water has benefit of being used for cooling purposes in nearly every industry. Thus, there is a wealth of information pertaining to water performance as a coolant and on designing water-cooled systems. Some benefits of using water as a coolant type are its relative abundance, ease of handling and filtration, moderation effect upon neutrons, high heat transfer capacity with phase change, minimum environmental and personal safety concerns and compatibility with most tubing materials. A major safety concern with using water as a coolant is voiding effects. Fission reactor operating experiences show that system temperatures above the departure from nucleate boiling range result in significant water voiding. Water voiding represents a loss of heat removal efficiency since the water is coalescing into bubbles or voids and the entrapped steam has a low thermal conductivity. Consequently, coolant voiding may cause localized hot spots in the

* Corresponding author at: Atomic Energy Authority, Cairo, Egypt.
Tel.: +20 18 9752796.
E-mail address: selmorshedy@etrr2-aea.org.eg (S.E.-D. El-Morshedy), hassanein@purdue.edu (A. Hassanein).

0920-3796/$ – see front matter © 2009 Published by Elsevier B.V.
doi:10.1016/j.fusengdes.2009.02.051

Nomenclature

A	channel flow area (m^2)
Cp	specific heat at constant pressure (J/kg K)
D	channel diameter (m)
D_e	equivalent hydraulic diameter (m)
D_h	heated diameter (m)
F_0	channel friction factor
F_{st}	friction factor for swirl tape channel
G	mass flux (kg/m^2 s)
h	heat transfer coefficient (W/m^2 °C)
I	enthalpy (J/kg)
I_{fg}	latent heat of evaporation (J/kg)
k	thermal conductivity (W/m °C)
L	active length (m)
Nu	Nusselt number = hD_e/k
P	pressure (Pa)
Pr	Pradentl number = $\mu Cp/k$
Re	Reynolds number = GD_e/μ
q	volumetric heat generation (W/m^3)
T	temperature (°C)
u	coolant velocity (m/s)
v	specific volume (m^3/kg)
W	divertor width (m)
H	divertor height (m)
x	distance in radial horizontal direction (m)
x	steam quality
y	distance in radial vertical direction (m)
z	distance in axial direction (m)

Greek letters

α	thermal diffusivity (m^2/s)
δ	swirl tape thickness (m)
ρ	density (kg/m^3)
μ	dynamic viscosity (kg/ms)
σ	surface tension (N/m)
Φ	surface heat flux (W/m^2)
τ	time (s)

Superscripts

p	time step index
*	means dimensionless quantity

Subscripts

c	coolant
CHF	critical heat flux
fg	difference of saturated liquid and vapor
g	vapor phase
in	inlet
l	liquid phase
NCB	nucleate boiling contribution
ONB	onset of nucleate boiling
out	outlet
sat	saturated
SP	single phase
st	swirl tape
TP	two-phase
w	wall

tubing, which in turn may result in a loss of the tube's mechanical integrity. However, the probability of water voiding can be greatly reduced by using water in its subcooled state. Through controlled pressurization of water, its temperature will be sufficiently below the saturation temperature at the given pressure. Thus, significant heat must be absorbed by the water before voiding can commence. At 4 MPa pressure and an inlet temperature of 150 °C, ITER has an approximate subcooling of 100 °C. During normal operations, this level of subcooling should circumvent any voiding concerns. The prediction of the thermal response of the divertor components is a major concern for both the thermal-hydraulic design and safety analysis of the reactor. Therefore, the objective of the present work is to develop a model to simulate cooling processes of the ITER divertor in both normal and off-normal operation. The model is entitled ITERTHA (International Thermonuclear Experimental Reactor Thermal Hydraulic Analysis).

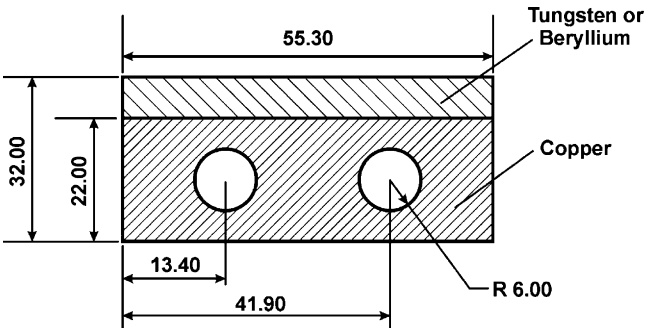

Fig. 1. ITER divertor schematic (dimensions in mm).

2. Model description

Fig. 1 is a typical schematic design of ITER divertor. The structural material is copper coated by tungsten or beryllium with water being the coolant. Due to similarity around the vertical axis, the present model will focus on only one half of the divertor module in which only one coolant channel. The coolant channel is divided into a specified axial regions while both the divertor and armour are divided into a two-dimension mesh in the radial direction, then a nodal thermal-hydraulic calculation for coolant, divertor and armour is performed with a uniform incident heat flux on the armour surface.

2.1. Coolant temperature

The model treats the coolant as one lumped node. It thus assumed that the coolant is well stirred and has a uniform temperature. The coolant channel is divided into a given number of elements in the axial z-direction where the general energy balance equation is applied to each element:

$$\rho A\,\Delta z\frac{dI(\tau)}{d\tau} = \int_0^{2\pi} \phi(\tau,\theta)d\theta\, R\Delta z + G(\tau)A(I_{in}(\tau) - I_{out}(\tau)) \quad (1)$$

where A is the channel cross-sectional area, $\phi(\tau,\theta)$ is the wall heat flux at time τ and radial angle θ, R is the coolant channel radius, $G(\tau)$ is the coolant mass flux at time τ, and $I(\tau)$ is the coolant enthalpy at time τ.

2.2. Divertor temperature

The temperature distribution through the divertor is governed by the two-dimensional general heat conduction equation that takes the following form in Cartesian coordinates:

$$\rho Cp\frac{dT}{d\tau} = \frac{\partial}{\partial x}\left(k(T)\frac{\partial T}{\partial x}\right) + \frac{\partial}{\partial y}\left(k(T)\frac{\partial T}{\partial y}\right) + q(x,y,\tau) \quad (2)$$

Based on the finite difference technique, the model solves the heat conduction in the mesh nodes of a half divertor plate in two-dimensional explicit scheme. Twenty equations are derived from

the general conduction equation to cover all the mesh points. One for each corner, one for each side, one for the interior points, one for the nodes on the line of interface between the two materials and one at the beginning and another one at the end of this line. Also, the perimeter of the coolant channel is divided into four segments; each segment has its own equation with a convection boundary where the heat transfer coefficient is determined at each node. There is also one equation for each node connecting two segments. The number of elements in Z direction and points in X and Y directions are input and so any mesh size can be used. The armour mesh is divided into two different size meshes to enable choosing a smaller mesh size at the upper part of the armour and so the model accounts for evaporation more accurate. The time step is also an input but it varies if necessary during calculation to satisfy the numerical stability condition. In this work 25 elements is chosen in Z direction, 100 points in X direction and 160 points in Y direction (100 for Cu and 60 for Be or W). If the armour cell temperature reaches the melting temperature, a quantity of the deposited energy equal to the latent heat of fusion is consumed to convert the armour material from solid to liquid states. After energy deposition phase and as soon as the cell temperature reaches the melting temperature a similar quantity of heat is removed from the cell to convert it from liquid to solid state. Once melting commences in the cell where the cells below this cell are in solid phase and the cells above it are in liquid phase, the melt–solid cell temperature is fixed until all the heat of fusion is either absorbed to change to liquid phase or removed to change to the solid phase according to the following equation:

$$\rho H_f \frac{dy}{d\tau} = k_s \frac{\partial T_s}{\partial y} - k_l \frac{\partial T_l}{\partial y} \tag{3}$$

where H_f, k_s and k_l are the latent heat of fusion, the thermal conductivity of the solid phase and the thermal conductivity of the liquid phase, respectively.

The model also accounts for the heat removed through armour material due to evaporation. The kinetics of evaporation establishes the connection between the surface temperatures and the net atom flux leaving the surface. Since the maximum temperature will be at the surface, no boiling phenomenon is assumed to take place. Consequently, there is no specific temperature where a phase change from liquid to vapor phase can occur. Rather there is a continuous flow of vaporized atoms in which the rate of material removal depends only on the surface temperature, the corresponding vapor pressure and the type of the wall material.

The quantity of heat consumed for evaporation in a time $d\tau$ is

$$dq_{ev} = \rho v(\tau) h_{ev} d\tau \tag{4}$$

where h_{ev} is the latent heat of evaporation, and $v(\tau)$ is the velocity of the receding surface and given in cm/s by [3]:

$$v(\tau) = 5.8 \times 10^{-2} \frac{\alpha\sqrt{A} P_v(T)}{\rho(T)\sqrt{T}} [0.8 + 0.2 e^{-\tau/10\tau_c}] \tag{5}$$

where α is sticking probability (usually = 1), A is atomic mass number, P_v is vapor pressure (Torr) and τ_c is vapor collision time (s).

2.3. Coefficient of heat transfer

The model calculates the heat transfer coefficient for both the single-phase and the boiling two-phase flow. The model first defines the flow regime at each axial node and then performs calculations to obtain the heat transfer coefficient as follows.

2.3.1. Single-phase forced convection

(a) Turbulent regime $Re \geq 10{,}000$; Dittus–Boelter [4] equation is used:

$$Nu = 0.023\ Re^{0.8} Pr^{0.4} \tag{6}$$

(b) Transition regime $2100 < Re < 10{,}000$; Nusselt number is calculated by interpolation between the laminar and turbulent correlations.

(c) Forced laminar regime $Re \leq 2100$; Sieder and Tate [5] correlation is used:

$$Nu = 1.86 \left(\frac{Re\ Pr}{L/D_e} \right)^{1/3} \left(\frac{\mu_c}{\mu_w} \right)^{0.14} \tag{7}$$

2.3.2. Subcooled boiling

Boiling is initiated when the coolant channel wall temperature is equal to the onset of nucleate boiling temperature, T_{ONB}, where

$$T_{ONB} = T_{sat} + (\Delta T_{sat})_{ONB} \tag{8}$$

where $(\Delta T_{sat})_{ONB}$ is given by Bergles and Rohsenow correlation [6] which is valid for water only over the pressure range 1–138 bar:

$$(\Delta T_{sat})_{ONB} = 0.556 \left\{ \frac{\phi_{ONB}}{1082 P^{1.156}} \right\}^{0.463 P^{0.0234}} \tag{9}$$

where P is the local pressure in bar and ϕ_{ONB} is in W/m^2.

The correlation developed by Chen [7] for saturated boiling as described subsequently is extended for use in the subcooled boiling. It is assumed that the total heat flux is made up of a nucleate boiling contribution and a single phase forced convective contribution

$$\phi(z) = h_{NCB}(T_w(z) - T_{sat}(z)) + h_{SP}(T_w(z) - T_c(z)) \tag{10}$$

where h_{SP} is calculated as described above in Section 2.3.1 and h_{NCB} is calculated for saturated boiling detailed in the next section.

2.3.3. Saturated nucleate boiling

The heat transfer coefficient in forced flow saturated boiling is estimated by the correlation proposed by Chen [7]:

$$h_{TP} = h_{SP} + h_{NCB} \tag{11}$$

$$h_{SP} = 0.023 \left[\frac{G(1-x)D_e}{\mu_l} \right]^{0.8} \left[\frac{\mu Cp}{k} \right]_l^{0.4} \left(\frac{k_l}{D_e} \right) (F) \tag{12}$$

F is the convective boiling enhancement factor and calculated as

$$F = \begin{cases} 1.0 & \text{for} \quad 1/X_{tt} \leq 0.1 \\ 2.35(1/X_{tt} + 0.213)^{0.736} & \text{for} \quad 1/X_{tt} > 0.1 \end{cases} \tag{13}$$

where X_{tt} is the Lockhart-Martinelli parameter and given by

$$X_{tt} = \left(\frac{1-x}{x} \right)^{0.9} \left(\frac{\rho_g}{\rho_l} \right)^{0.5} \left(\frac{\mu_l}{\mu_g} \right)^{0.1} \tag{14}$$

$$h_{NCB} = 0.00122 \left[\frac{k_l^{0.79} Cp_l^{0.45} \rho_l^{0.49}}{\sigma^{0.5} \mu_l^{0.29} I_{fg}^{0.24} \rho_g^{0.24}} \right] \Delta T_{sat}^{0.24} \Delta P_{sat}^{0.75} (S) \tag{15}$$

where ΔT_{sat} is the wall superheat, ΔP_{sat} is the difference between the saturation pressures calculated from the wall temperature and the fluid temperature and S is the nucleate boiling suppression factor and calculated as

$$S = \begin{cases} [1 + 0.12 Re_{TP}^{1.14}]^{-1} & \text{for} \quad Re_{TP} < 32.5 \\ [1 + 0.42 Re_{TP}^{0.78}]^{-1} & \text{for} \quad 32.5 < Re_{TP} < 70 \end{cases} \tag{16}$$

Re_{TP} is the two-phase Reynolds number and given by

$$Re_{TP} = Re_l \times F^{1.25} \tag{17}$$

2.3.4. Transition film boiling

In order to calculate the critical heat flux, the Tong-75 correlation [8] is used as it satisfactorily incorporates the thermal and hydrodynamic effects associated with the onset and progression of

CHF. Its predictions for the local CHF has been recommended for fusion CHF as it compares well with experimental data

$$\phi_{CHF} = 0.23 f_0 G I_{fg} (1 + 0.00216 P_{ratio}^{1.8} Re^{0.5} Ja) \quad (18)$$

where f_0 is the Fanning friction factor, $f_0 = 8.0\, Re^{-0.6} D_{ratio}^{0.32}$; $D_{ratio} = D_e/D_0$, D_e is the hydraulic diameter and D_0 is a reference diameter = 0.0127 m; $P_{ratio} = P/P_c$, P is the local pressure and P_c is the critical pressure = 22.1 MPa; Ja is the Jakob number, $Ja = -X_{sub}(\rho_l/\rho_g)$ and X_{sub} is the quality of subcooled liquid, $X_{sub} = -Cp\Delta T_{sub}/I_{fg}$.

As the wall temperature reaches the CHF temperature (the wall temperature at a heat flux = ϕ_{CHF}) the model calculates the heat transfer coefficient using Marshall-98 correlation [9] as it demonstrated agreement with data from fusion-relevant experiments

$$\phi = \phi_{CHF} \left(\frac{T_w - T_{sat}}{T_{CHF} - T_{sat}} \right)^{-0.23}. \quad (19)$$

2.4. Heat transfer enhancement

Due to the extremely high heat flux values in fusion reactors, a heat transfer enhancement technique is required in order to achieve a sufficient margin on critical heat flux at a reasonable flow velocity. The usage of swirl tapes in flow boiling experiments were performed in 1962 [10] for pressurized water reactor studies at Argonne National Laboratory. This and subsequent research reveal that swirl tap inserts in the coolant channels significantly increase the heat transfer coefficient in forced convection regime [11]. The swirl tape inserts influence on the fully developed nucleate boiling regime is negligible; however, they considerably increase the critical heat flux [12]. When the cooling channel features a swirl tape insert, swirl tape factors must be applied to the previously described heat transfer correlations that were defined for bare channel tubes [13].

2.4.1. Forced convection heat transfer

The value of Nusselt number given in Section 2.3.1 is multiplied by the swirl tape modification of Lopina and Bergles [14] as follows:

$$Nu_{st} = Nu \times 2.26 Y^{-0.248} \quad (20)$$

where Y is the swirl tape ratio, defined as the number of tube inner diameters per the pitch length for 180° rotation of the tape.

2.4.2. Critical heat flux

The critical heat flux correlation for bare tubes (Tong-75 correlation) is also used for swirl tape tubes after modifying its friction factor to account for the swirl tape inserts. Lopina and Bergles [14] correlate their experimental data to obtain a new friction factor in the following equation:

$$f_{st} = f_0 \times [2.75 Y^{-0.406}] \quad (21)$$

where f_{st} is the friction factor for swirl tape tube.

For swirl tape tubes the concept of the equivalent hydraulic diameter should be applied to all the previous heat transfer correlations while the concept of the heated diameter should be applied to the energy equation. In this model, the concept of both the hydraulic and heated diameters are used precisely and no other factors implemented in the swirl tape correlations as done in previous work [13]. The equivalent hydraulic diameter takes the following form:

$$D_e = 4 \times \left[\frac{(\pi D^2/4) - \delta D}{\pi D + 2(D - \delta)} \right] \quad (22)$$

While the heated diameter takes the following form:

$$D_h = 4 \times \left[\frac{(\pi D^2/4) - \delta D}{\pi D - 2\delta} \right] \quad (23)$$

where δ is the tape thickness.

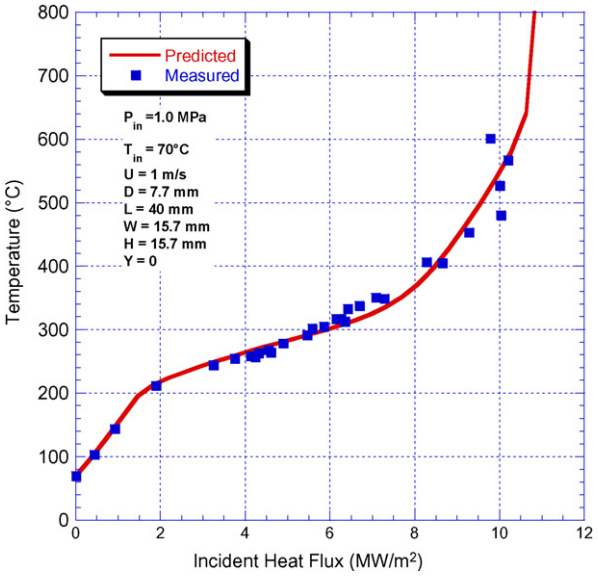

Fig. 2. Predicted and measured surface temperatures for bare channel mockup with coolant velocity = 1 m/s.

3. Model validation

The present model is validated by experiments performed at Sandia National Laboratory by Marshall [13] and [15] for two prototypical International Thermonuclear Experimental Reactor (ITER) divertor channels for both bare channel and swirl tape channel mockups. The thermocouples are located at 0.6 mm depth of the cupper surface for both mockups. The experimental data is obtained under both normal steady state operating conditions and transient off-normal situation during simulated loss of flow accident (LOFA).

3.1. Steady state validation

Figs. 2–4 show a comparison between the surface temperatures predicted by the present model and the measured values of the bare channel mockup under different heat fluxes and consequently

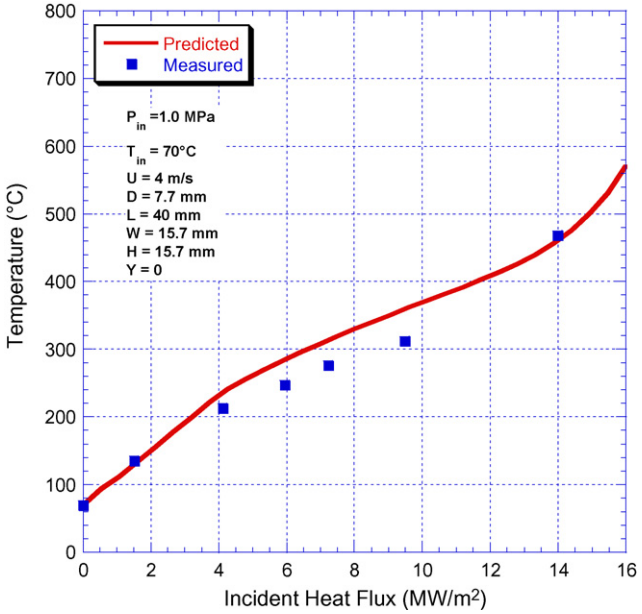

Fig. 3. Predicted and measured surface temperatures for bare channel mockup with coolant velocity = 4 m/s.

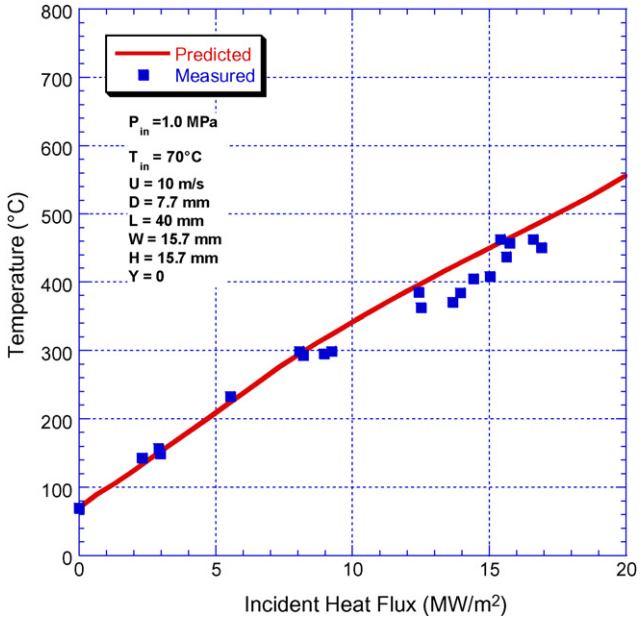

Fig. 4. Predicted and measured surface temperatures for bare channel mockup with coolant velocity = 10 m/s.

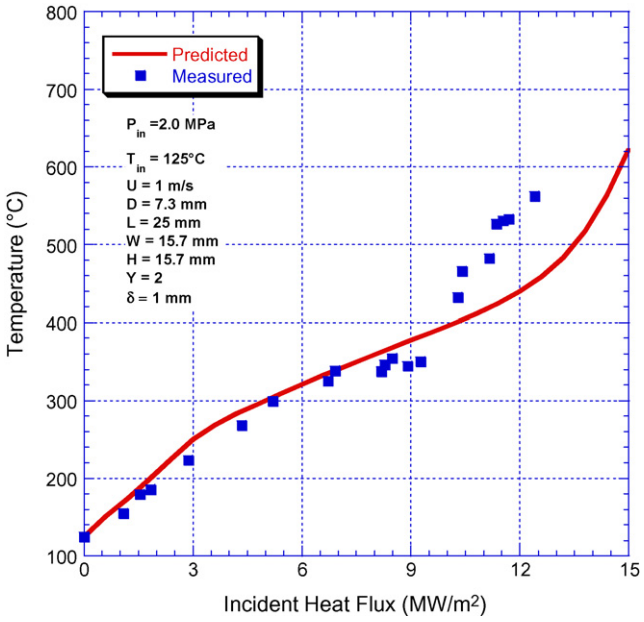

Fig. 6. Predicted and measured surface temperatures for swirl tape channel mockup under pressure of 2 MPa.

different heat transfer regimes. The comparison is performed under the following conditions:

(1) coolant inlet pressure = 1 MPa
(2) coolant inlet temperature = 70 °C
(3) coolant velocity = 1, 4, and 10 m/s
(4) coolant channel diameter = 7.7 mm
(5) mockup length = 40 mm
(6) mockup width = 15.7 mm
(7) mockup height = 15.7 mm

The comparison reveals that the developed model predictions give a very good agreement with experimental data.

Figs. 5–7 show the surface temperature predictions and the measured values of the swirl tape channel mockup. The comparison is performed under the following conditions:

(1) coolant inlet pressure = 1, 2, and 4 MPa
(2) coolant inlet temperature = 70 °C
(3) coolant velocity = 1 m/s
(4) coolant channel diameter = 7.3 mm
(5) mockup length = 30 mm
(6) mockup width = 15.7 mm
(7) mockup height = 15.7 mm
(8) swirl tape ratio = 2
(9) swirl tape thickness = 1 mm

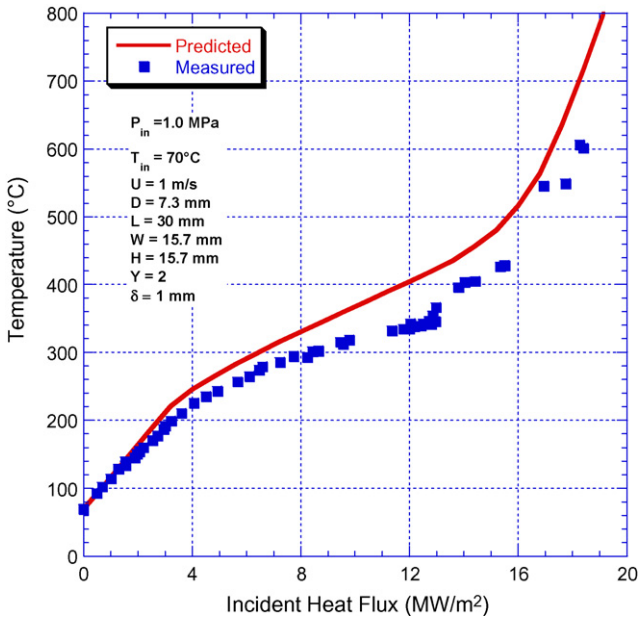

Fig. 5. Predicted and measured surface temperatures for swirl tape channel mockup under pressure of 1 MPa.

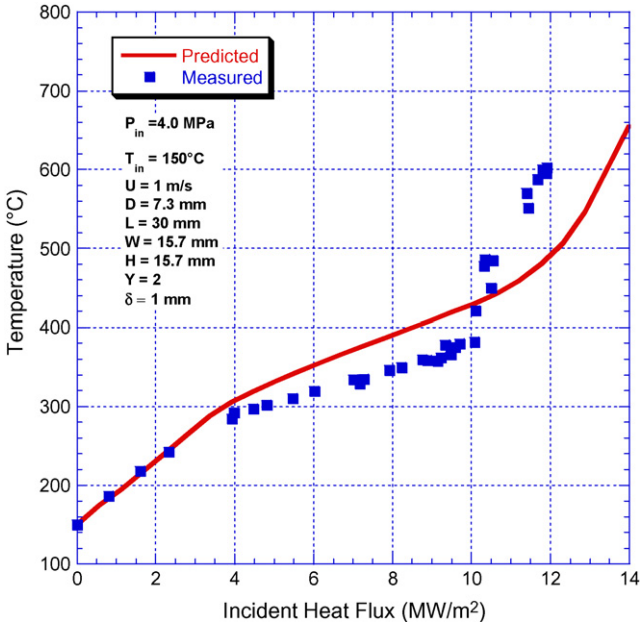

Fig. 7. Predicted and measured surface temperatures for swirl tape channel mockup under pressure of 4 MPa.

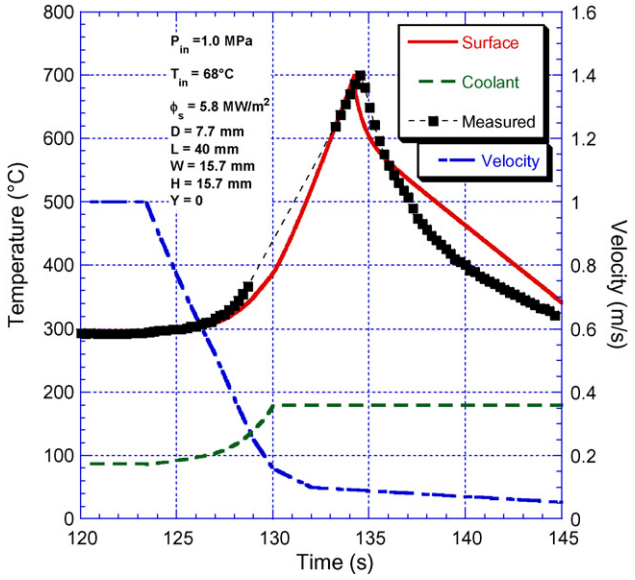

Fig. 8. Predicted and measured surface temperatures for bare channel mockup under LOFA experiment.

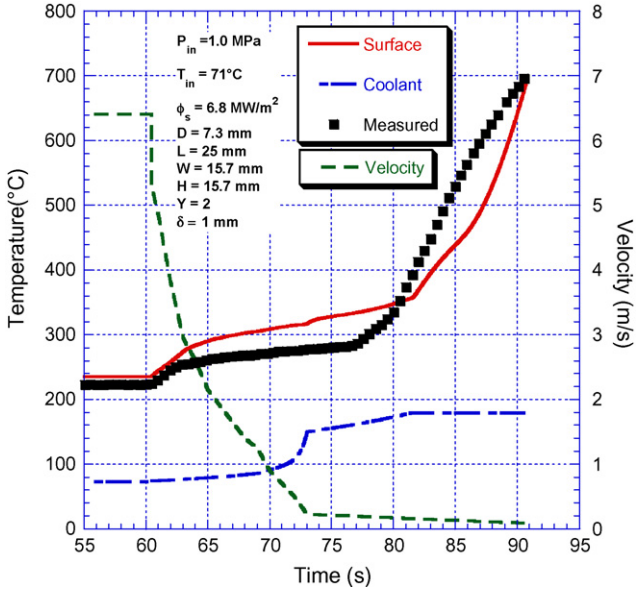

Fig. 9. Predicted and measured surface temperatures for swirl tape channel mockup under LOFA experiment.

It also shows a good agreement with the experimental data. However, at higher heat fluxes more than 8 MW/m^2, a transition film boiling regime achieved and so the quantity of heat transfer decreased exponentially. Therefore, any small deviation in the prediction of the onset of the critical heat flux phenomenon leads to a considerable deviation in the temperature values. It means that the swirl tape factor used in the critical heat flux correlation needs more justification. The results also show how the swirl tape inserts enhances the critical heat flux and so the mockup can withstand higher heat fluxes before burn out.

3.2. Transient validation

The present model is used to simulate the loss of flow experiments performed at Sandia National Laboratory on ITER mockups for both bare and swirl tape coolant channels. Fig. 8 shows both the predicted and measured temperatures for the bare channel mockup under LOFA experiment. The pump coast down starts at time = 123.42 s while uniform heating of the mockup continues until a high temperature trip occurs at 700 °C. The comparison is performed under the following conditions:

(1) coolant inlet pressure = 1 MPa
(2) coolant inlet temperature = 70 °C
(3) coolant channel diameter = 7.7 mm
(4) mockup length = 40 mm
(5) mockup width = 15.7 mm
(6) mockup height = 15.7 mm

As shown the predicted temperatures are in good agreement with the experimental data.

Fig. 9 shows both the predicted and measured temperatures for the swirl tape channel mockup under LOFA experiment. The pump coast down starts at time = 60.44 s while uniform heating of the mockup continued until a high temperature trip occurs at 700 °C. The comparison is performed under the following conditions:

(1) coolant inlet pressure = 1 MPa
(2) coolant inlet temperature = 71 °C
(3) coolant channel diameter = 7.3 mm
(4) mockup length = 30 mm
(5) mockup width = 15.7 mm
(6) mockup height = 15.7 mm
(7) swirl tape ratio = 2
(8) swirl tape thickness = 1 mm

The predicted temperatures in this case are also in good agreement with the experimental data.

4. Results and discussion

The present model is used to simulate the thermal response of ITER divertor exposed to a plasma vertical displacement event (VDE). The initial phase prior to VDE is characterized by unheated divertor with inlet coolant temperature = 71 °C. It is assumed that all temperature values through are equal to the inlet coolant temperature. At time $\tau = 0$, the plasma deposits parts of its energy about

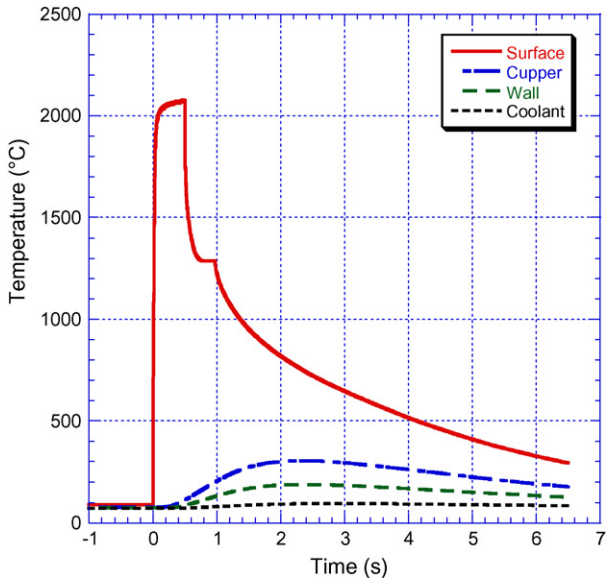

Fig. 10. Divertor temperatures under 60 MJ/m^2 energy deposition in 0.5 s for 10 mm Be armour.

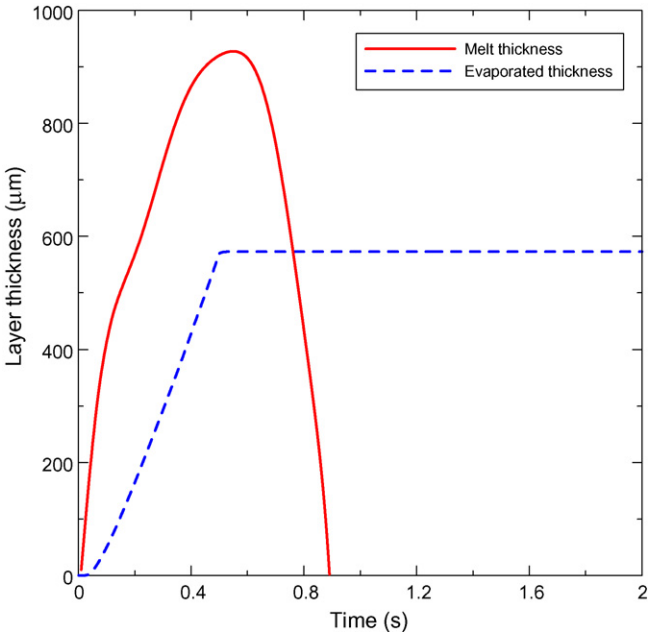

Fig. 11. Melt and evaporated layer thickness during VDE for 10 mm Be armour.

60 MJ/m^2 during 0.5 s leading to a high heat flux of 120 MW/m^2 on divertor surface. Therefore, the temperature rises rapidly in the surface region until the melting point is reached. Then, the melt–solid interface continues to move deeper into the armour while the temperature continues to rise in the melted surface. Evaporation then intensifies from the melted surface until the net heat flux drops at the end of the VDE, i.e., $\tau = 0.5$ s. Then, the energy deposition into the divertor ceased and the hot melt layer cooled by evaporation, radiation, and conduction to the divertor coolant channels. The temperature of the melt surface becomes too low for further evaporation and resolidification of the melt layer takes place. All the results presented in the following figures are obtained at the end of the heated axial length.

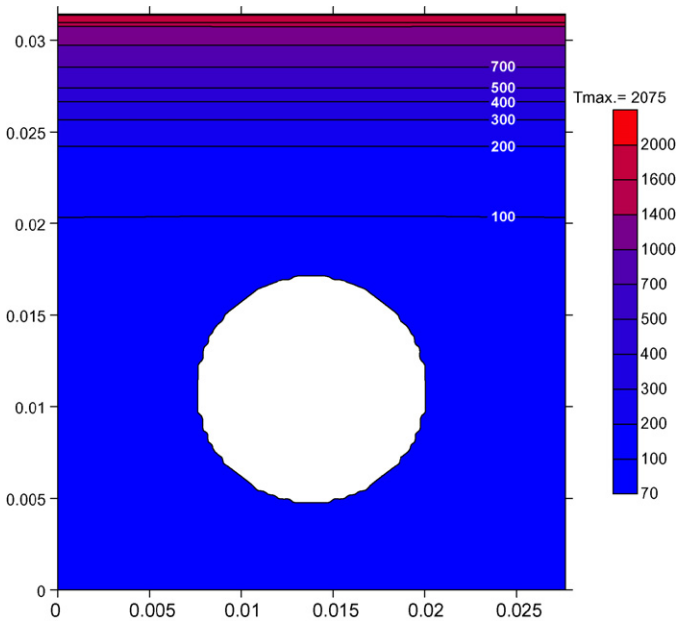

Fig. 12. Divertor temperature distributions at the end of the VDE for 10 mm Be armour.

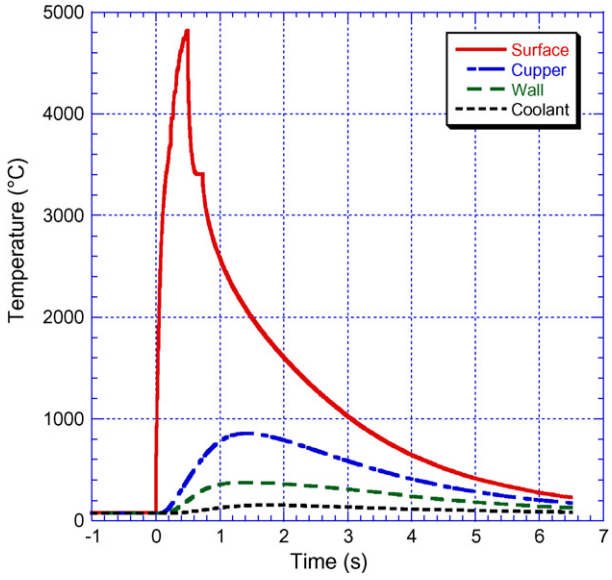

Fig. 13. Divertor temperatures under 60 MJ/m^2 VDE in 0.5 s for 10 mm W armour.

Fig. 10 shows the thermal behavior of the divertor with 10 mm beryllium armour under a VDE. The surface temperature increased sharply from the steady state value (71 °C) to more than 2000 °C in only 0.04 s, then the intense evaporation reduces the net energy deposited through beryllium and significantly suppresses the temperature rise. As soon as the VDE ends, the surface temperature falls rapidly mainly due to evaporation and conduction until reaching the beryllium melting temperature, 1287 °C where the melted beryllium loses its latent heat of fusion before resolidifying. Then beryllium temperature decreases due to cooling through the divertor channel. Fig. 11 shows the variation of both the melted and evaporated layer thickness due to plasma energy deposition. The beryllium armour starts to melt after about 15 ms and the melt layer thickness increases to more than 900 μm by the end of VDE, then the temperature decreased leading the melt layer to rapidly resolidify. The evaporation layer thickness increases linearly to reach

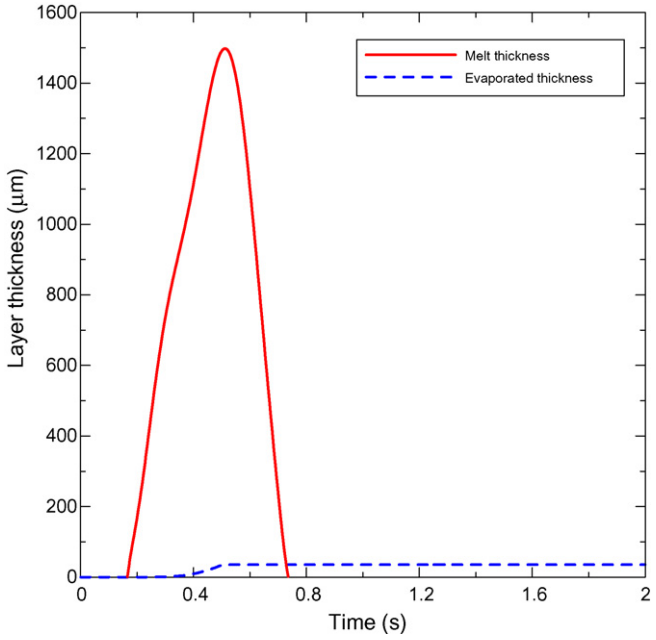

Fig. 14. Melt and evaporated layer thickness during VDE for 10 mm W armour.

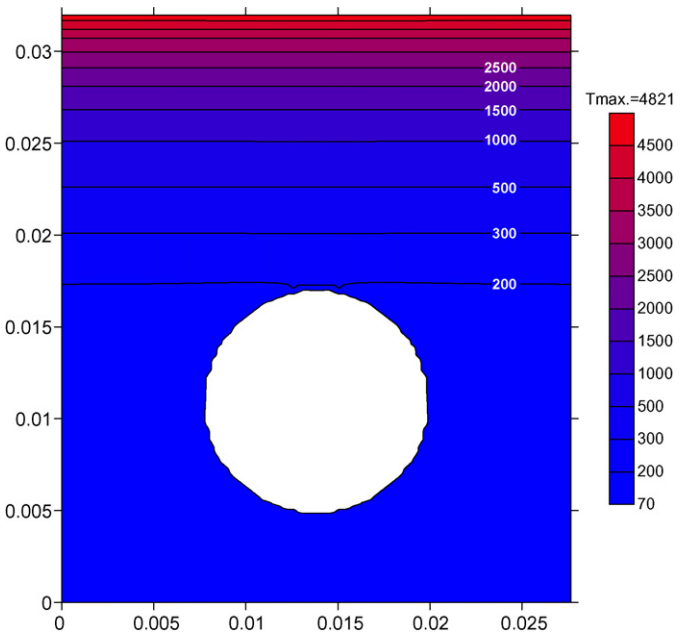

Fig. 15. Divertor temperature distributions at the end VDE for 10 mm W armour.

about 570 μm by the end of the VDE. Fig. 12 shows a contour plot of the temperature distribution through the divertor with 10 mm beryllium armour at the end of the VDE.

Fig. 13 shows a simulation of VDE when using 10 mm tungsten armour. In this case, higher surface temperatures are predicted as the melting temperature of tungsten is higher (3407 °C) and the evaporation rate becomes significant above 4000 °C surface temperature. After VDE, the temperature decreases to lower values than in case of beryllium armour due to the relatively higher thermal conductivity of tungsten.

Fig. 14 shows the variation of both the melt and evaporated layer thickness due to plasma energy deposition. The tungsten melt layer thickness slightly exceeds 1500 μm before resolidification starts after the VDE duration while the evaporation thickness reaches only 35 μm.

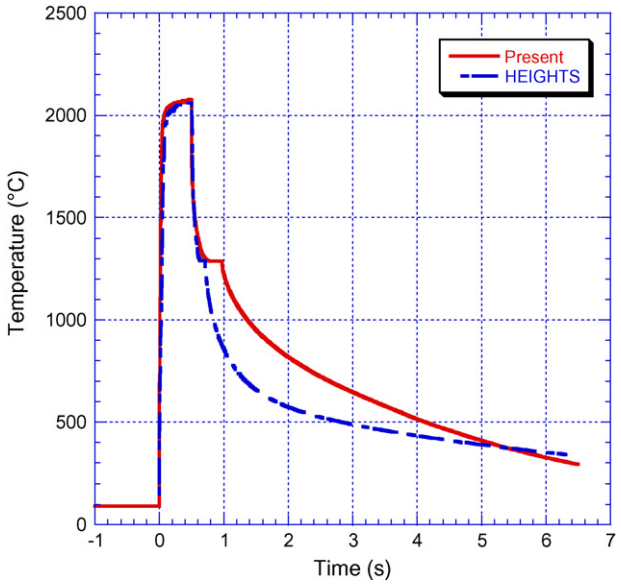

Fig. 16. Surface temperature predicted by the present model and HEIGHTS for 10 mm Be armour.

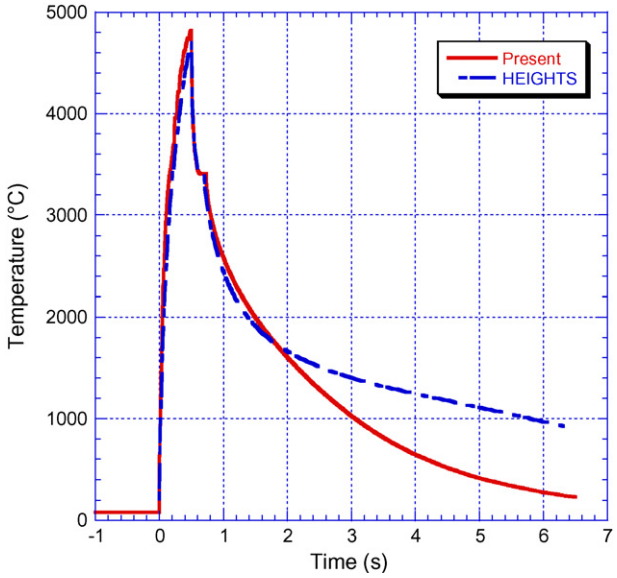

Fig. 17. Surface temperature predicted by the present model and HEIGHTS for 10 mm W armour.

Fig. 15 shows a contour plot of the temperature distribution through the divertor with 10 mm tungsten armour at the end of the VDE. The divertor temperatures have higher values in this case due to the higher melting temperature of tungsten.

Figs. 16 and 17 show the surface temperature predicted by the present model and the comprehensive HEIGHTS [16] package under 60 MJ/m^2 energy deposition in 500 ms for both beryllium and tungsten armours, respectively. There is a good agreement in the region where the heat transfer by evaporation is dominant, and then deviation occurs due to the difference in the used heat transfer models. The methodology of predicting the coolant temperature is the main responsible for this deviation where in HEIGHTS [17,18] a time-dependent thermal balance is used while the energy equation is used in the present model in which the rate of change in enthalpy along each axial element is accounted for and the heat flux used is the average channel wall heat flux at each axial element (Eq. (1)). The variation in the coolant temperature leads to a different heat transfer regimes which in turn leads to a higher deviation in both the coolant channel wall and divertor surface temperatures.

5. Conclusion

A computer program entitled ITERTHA (International Thermonuclear Experimental Reactor Thermal Hydraulic Analysis) has been developed to simulate the thermal-hydraulic behavior of ITER divertor modules under both steady and transient states. The selected heat transfer correlations cover all possible operating conditions of ITER for both normal and off-normal plasma events. Melting, vaporization, and solidification of the armour material are accounted for. The present model is validated by experimental data performed at Sandia National Laboratory for both bare and swirl tape coolant channel mockups and shows a good agreement with the experimental data during both the steady and transient states. The model is used to simulate ITER divertor thermal response under intense transient energy deposition of vertical displacement events. This VDE of 60 MJ/m^2 deposited in 500 ms leads to a maximum surface temperature of 2070 °C and 4800 °C for both beryllium and tungsten armours, respectively. However, the maximum copper temperatures remain below the melting point, the maximum coolant channel wall temperatures remain below the burnout temperature and the maximum coolant temperatures remain below

saturation temperature by good margins for both beryllium and tungsten armour cases. As a result of the VDE, 570 μm of the beryllium armour is evaporated while only 35 μm of the tungsten armour is evaporated. The surface temperature predicted by the present model in this case is also compared with HEIGHTS predictions with a very good agreement is achieved during the deposition period while a slight deviation is predicted after the end of VDE due to the variation of the heat transfer models used in both programs.

Acknowledgment

This work is supported by the U.S. Department of Energy, Office of Fusion Energy Sciences.

References

[1] Draft Report for ITER Concept Definition Phase, IAEA, ITER Technical Report, 1989.
[2] T. Kuroda, G. Vieider, ITER Plasma Facing Components, ITER Documentation Series, 30, IAEA, Vienna, 1990.
[3] A.M. Hassanein, G.L. Kulcinski, Simulation of rapid heating in fusion reactor first wall using the Green's function approach, ASME 106 (August) (1984) 486–490.
[4] F.W. Dittus, L.M.K. Boelter, University of California, Berkeley, Publications on Engineering, vol. 2, p. 443, 1930.
[5] E.N. Sieder, G.E. Tate, Ind. Eng. Chem. 28 (1429) (1936).
[6] J.G. Collier, Convective Boiling and Condensation, Second edition, Mc Graw-Hill Internal Book Company, 1981.
[7] J.C. Chen, A correlation for Boiling Heat Transfer to Saturated Fluids in Convective Flow, Ind. Eng. Chem. Process Des. Dev. 5 (3) (1966) 322–329.
[8] L.S. Tong, A phenomenological study of critical heat flux, ASME paper, 75-HT-68.
[9] J.A. Koski, R.D. Watson, A.M. Hassanein, P.L. Goranson, J.C. Salmonson, Thermal-hydraulic design issues and analysis for the ITER divertor, Fusion Technol. 19 (1991) 1729–1735.
[10] R. Viskanta, Critical heat flux for water in swirling flow, Nucl. Sci. Eng. 10 (2) (1961) 202.
[11] R.M. Manglik, A.E. Bergles, Heat transfer and pressure drop correlations for twisted-tape inserts in isothermal tubes. Part I. Laminar flows, J. Heat Transf. 115 (1993) 881–896.
[12] D.P. Shatto, G.P. Peterson, A review of flow boiling heat transfer with twisted-tape inserts, J. Enhanc. Heat Transf. 3 (4) (1996) 233–257.
[13] T.D. Marshall, Experimental examination of the post-critical heat flux and loss of flow accident phenomena for prototypical ITER divertor channels, PhD Thesis, Rensselaer Polytechnic Institute, Troy, New York, 1998.
[14] R.F. Lopina, A.E. Bergles, Heat transfer and pressure drop in tape-generated swirl flow of single phase water, J. Heat Transf. 91 (8) (1969) 434–442.
[15] T.D. Marshall, J.M. McDonald, L.C. Cadwallader, D. Steiner, An experimental examination of the loss of flow accident phenomenon for prototypical ITER divertor channels of Y = 0 and Y = 2, Fusion Technol. 37 (2000) 38–53.
[16] A. Hassanein, Prediction of material erosion and lifetime during major plasma instabilities in Tokamak devices, Fusion Eng. Des. 60 (2002) 527–546.
[17] A. Hassanein, T. Sizyuk, Comprehensive simulation of vertical plasma instability events and their serious damage to ITER plasma facing components, Nucl. Fusion 48 (2008), 115008 (11pp).
[18] A. Hassanein, T. Sizyuk, M. Ulrickson, Vertical displacement events: a serious concern in future ITER operation, Fusion Eng. Des. 83 (2008) 1020–1024.